HELIOSEISMIC CONSTRAINTS ON THE STRUCTURE OF THE SOLAR TACHOCLINE

P. Charbonneau
High Altitude Observatory, National Center for Atmospheric Research[1],
P.O. Box 3000, Boulder, CO80307-3000, U.S.A.

J. Christensen-Dalsgaard
Institut for Fysik og Astronomi, Aarhus Universitet,
DK-8000 Aarhus C, Denmark

R. Henning
Dept. of Physics and Astronomy, University of Denver
2212 E. Wesley Ave., Denver, CO 80208, U.S.A.

J. Schou
Center for Space Science and Astrophysics, HEPL Annex 201,
Stanford University, Stanford, CA 94305-4085, U.S.A.

M.J. Thompson
Astronomy Unit, Queen Mary and Westfield College,
Mile End Road, London E1 4NS, U.K.

S. Tomczyk
High Altitude Observatory, National Center for Atmospheric Research,
P.O. Box 3000, Boulder, CO80307-3000, U.S.A.

e-mail: paulchar@hao.ucar.edu, jcd@obs.aau.dk, rhenning@du.edu,
schou@skaelv.stanford.edu, m.j.thompson@qmw.ac.uk, tomczyk@hao.ucar.edu

To be submitted to: *The Astrophysical Journal*

---

[1] The National Center for Atmospheric Research is sponsored by the National Science Foundation.

Abstract

1. Introduction

The first observational determination of the Sun's surface rotation were carried out by Fabricius, Galileo and Scheiner in the early decades of the seventeenth century. They did so using the newly invented astronomical telescope to follow, from day to day, the apparent motion of sunspots across the solar disc. It took another 250 years before R.C. Carrington established, again by tracking sunspots, that the surface solar rotation rate decreases with increasing heliospheric latitude, i.e., that the Sun's outer layers are in a state of *differential rotation*. Prior to the advent of helioseismology the solar *internal* differential rotation profile could only be inferred indirectly (for example through dynamo modeling), or computed by carrying out global numerical simulations of thermally-driven convection in a rotating, thick spherical shell, under various modeling assumptions. Most such simulations suggested that the solar internal rotation is approximately constant on concentric cylinder centered on the rotation axis. (see, e.g., Glatzmaier, 1985; Gilman & Miller, 1986; and references therein).

Shortly thereafter, the first helioseismic determinations of the latitude dependence of the solar internal angular velocity were carried out (Brown, 1985; Brown & Morrow, 1987) and indicated that the surface latitudinal observed on the solar surface persisted throughout the convective envelope, but vanished in the underlying radiative core ($r/R_\odot \lesssim 0.7$). These first studies could not rule out cylindrical rotation within the convective envelope. However, as helioseismic inferences of the solar internal rotation gained in accuracy over subsequent years, it became increasingly clear that at most latitudes, on the larger spatial scales there exists very little *radial* shear in the solar convective envelope. Instead, differential rotation therein is primarily latitudinal (i.e., $|r\partial\Omega/\partial r| \ll |\partial\Omega/\partial\theta|$), with the angular velocity at a given latitude approximately equal to its surface value (Brown *et al.*, 1989; Goode *et al.*, 1991). It also became apparent that the bulk of the radiative core is in a state of very near solid-body rotation (e.g., ; Tomczyk *et al.*, 1995; and references therein), the transition with the overlying differentially rotating envelope occurring across a thin ($\lesssim 0.1\,R_\odot$), approximately spherical layer often now referred to as the *solar tachocline* following the work of Spiegel & Zahn (1992).

From a dynamical point of view, the matching of a latitudinal gradient in angular velocity in the envelope to a rigidly rotating outer radiative core offers a challenging problem in stellar hydrodynamics. Approaching this problem from the standpoint of laminar hydrodynamics, Spiegel & Zahn (1992) have constructed tachocline models under the assumption of latitudinal geostrophic balance, and have shown that the helioseismically inferred thickness of the solar tachocline can only be reproduced if viscous momentum transport is strongly enhanced in the horizontal direction; otherwise, by the solar age radiative diffusion as well and angular momentum transport by the secondary meridional flow broadens the tachocline far beyond its inferred radial width (see also Elliott, 1997). They ascribe this enhanced horizontal transport to turbulence driven by shear instability of the differential rotation.

Alternately, Kitchatinov & Rüdiger (1993, 1995) have developed an analytical model for the (anisotropic) turbulent Reynolds stresses arising from the interaction between rotation and turbulence in the solar convective envelope, which also yields a steady-state differential rotation that is characterized by a tachocline-like shear layer immediately beneath the convective envelope (see Kitchatinov & Rüdiger 1995, Fig. 2). As in the Spiegel & Zahn model, their tachocline is far thicker than suggested by helioseismic inferences. They, however, suggest that magnetic stresses, rather than enhanced horizontal viscous coupling, are responsible for keeping the thickness of their tachocline in agreement with helioseismology inferences (Rüdiger & Kitchatinov, 1997).

The introduction of a magnetic field within the tachocline is far from being an *ad hoc* hypothesis. Based on studies of the stability and rise of toroidal magnetic flux ropes —presumed to give rise to sunspot pairs upon emerging through the photosphere,— it is becoming increasingly clear that the stably stratified layers located immediately beneath the convective envelope are the most likely location for the storage of magnetic flux (for a recent review see Schüssler, 1996). In such models, the stability properties of the magnetic flux ropes depends sensitively on the dynamical and thermodynamical structure of the storage layers, including of course its radial extent beneath the envelope.

Because of the strong radial shear present in its equatorial region, the solar tachocline is also a promising location for the seat of the solar dynamo. Thin layer mean-field dynamo models can and have been constructed (see, e.g., Rüdiger & Brandenburg, 199X, and references therein). A general property of such models is the dependence of the dynamo period on the thickness of the generating layer, reflecting the decrease of the magnetic dissipation time with decreasing thickness of the layer. A related class of dynamo models are the so-called *interface dynamos* (Parker, 1993; Tobias, 1996; Charbonneau & MacGregor, 1996, 1997), which are characterized by the spatial segregation of the shear and α-effect on either side of the core-envelope interface. Once again the behavior of the resulting dynamos is sensitively dependent on the thickness of the shear layer, and rely on the bulk of the shear layer being located in the upper part of the stably stratified radiative core, rather than at the base of the unstably stratified overlying envelope.

It is an intriguing and often unappreciated fact that the latitudinal shear profile in the solar convection zone is just about at the stability limit with respect to global, inviscid horizontal shear instability (Watson 1981). This would then imply that the underlying shear layer is everywhere hydrodynamically stable, since the latitudinal gradient therein decrease with depth. However, Gilman & Fox (1997) have shown that the simultaneous presence of toroidal magnetic fields and latitudinal differential rotation leads to a large-scale joint instability which manifest itself in the form of growing 2-D MHD waves of low azimuthal wavenumber. The existence of this instability has a number of interesting consequences from the point of view of magnetic field amplification and magnetic activity (see Gilman & Fox 1997 for a discussion). The important point to note here is that the occurrence of the instability depends on the bulk of the shear layer being stably stratified, otherwise flux removal by magnetic buoyancy occurs too rapidly for the instability to build up (among other problems).

The above discussion, however brief, is meant to highlights the fact that the true thickness of the solar tachocline, and its exact location with respect to the base of the convective envelope, are two extremely important quantities to determine observationally with the highest possible accuracy. Various helioseismic inversion experiments aimed specifically at this have been —and continue to be— devised. Using the Big Bear Solar Observatory 1986—1990 frequency splitting dataset in conjunction with a simple 2-parameter analytic form for the tachocline (central radius r_c and thickness w), Kosovichev (1996) finds $r_c/R_\odot = 0.692 \pm 0.005$ and $w/R_\odot = 0.09 \pm 0.04$. Along similar lines, from a limited set of forward modeling experiments using the LOWL data's a_3 splitting coefficients and a less constraining parameterization than that used by Kosovichev, Charbonneau *et al.* 1997 find $r_c/R_\odot = 0.704 \pm 0.003$ and $w/R_\odot = 0.0498 \pm 0.012$. Basu (1997) obtains very similar results using the GONG datasets and a different parameterization for the shear layer (see her Fig. 12 and accompanying discussion). Wilson, Burtonclay & Li (1997), however, find a somewhat deeper ($r/R_\odot = 0.68 \pm 0.01$) and thicker shear layer ($w/R_\odot \simeq 0.12$ —no error estimates given) with some latitudinal variation; the Kosovichev, Charbonneau *et al.*, and Basu determinations, on the other hand, assumed by construction a spherically symmetric tachocline.

While one may argue that the aforecited results are in reasonable agreement with one another, the differences in tachocline thickness are quite significant from the points of view of hydrodynamical structure, stability, and dynamo modeling. Consequently, the aim of this paper is to infer structural parameters for the tachocline —in particular its thickness— with the highest possible accuracy attainable using the LOWL frequency splitting dataset. We do so by computing a series of formal inversions and forward modeling solutions. The formal inversions are first presented and discussed in Section 2, with particular attention being put on the spatial resolution limits of the inversion methods. The forward modeling solutions are then presented in section 3, again after careful examination of the forward scheme's resolution limit. In Section 4 we investigate the possible latitudinal dependence of the tachocline structure, and conclude in Section 5 by assessing the consequences of our results for the various physical processes surveyed in this introduction and believed to operate in the vicinity of the core-envelope interface inside the Sun.

2. Formal Inversions

3. Forward Modeling

The results discussed in the preceding section suggest that the tachocline thickness is at or below the resolution limit of formal inversion methods. Consequently, we now describe a series of forward modeling experiments aimed specifically at accurately determining the tachocline thickness and location.

3.1 Parameterizations of the rotation profile

Rather than using a full 2-D discretization of the rotation profile $\Omega(r,\theta)$, the forward modeling approach followed here consists in expressing the rotation profile through a (nonlinear) parametric expression, and seek parameter values that give the best fit to the observed frequency splittings. Working in spherical polar coordinates (r,θ,ϕ), we write the (axisymmetric) rotation profile as:

$$\Omega(r,\theta;\Omega_c,\Omega_{\rm eq},c_1,c_2,r_c,w)=\Omega_c+f(r;r_c,w)(\Omega_S(\theta;\Omega_{\rm eq},c_1,c_2)-\Omega_c), \qquad (11)$$

where

$$\Omega_S(\theta;\Omega_{\rm eq},c_1,c_2)=\Omega_{\rm eq}+c_1\cos^2(\theta)+c_2\cos^4(\theta) \qquad (12)$$

defines the surface latitudinal differential rotation, and the function $f(r)$ is chosen to ensure a smooth transition between the rigidly rotating core (at rate Ω_c) and the surface. In what follows we use

$$f(r;r_c,w)=\frac{1}{2}\left[1+\mathrm{erf}\left(\frac{2(r-r_c)}{w}\right)\right] \qquad (13)$$

This describes a transition layer having the form of a spherical shell of central radius r_c, and of thickness $\simeq w$. More accurately, the corresponding radial shear $\partial\Omega/\partial r$ has the form of a Gaussian profile, with full width at half maximum equal to w. The rotation curve is then fully defined by the parameter set:

$$\mathbf{a}\equiv[\Omega_c,\Omega_{\rm eq},c_1,c_2,r_c,w] \qquad (14)$$

For a given such parameter set it is possible to compute, by a direct forward calculation, the frequency splitting coefficients $a_s(n, l; \mathbf{a})$ associated with the corresponding rotation curve (eqs. [11]—[13]):

$$a_s(n, l; \mathbf{a}) = \int \int K_{nls}(r, \theta)\Omega(r, \theta; \mathbf{a}) r \mathrm{d}r \mathrm{d}\theta, \qquad s \text{ odd} \tag{15}$$

where, for a given solar structural model, the Kernels K_{nls} are known quantities. The modeling task then consists in finding the parameter set $\mathbf{a}^*$ that minimizes the difference between the $a_s(\mathbf{a})$ computed via eq. (15) and the observed splitting coefficients a_s^{obs}. This is usually carried out by minimizing a normalized χ^2 measure:

$$\chi^2(\mathbf{a}) = \frac{1}{\nu} \sum_{n,l,s} \left(\frac{a_s(n, l; \mathbf{a}) - a_s^{\mathrm{obs}}(n, l)}{\varepsilon_{nls}} \right)^2 \tag{16}$$

with respect to the parameter set $\mathbf{a}$, although other statistical estimators of goodness-of-fit can also be used. The ε_{nls} in eq. (6) are observationally determined errors on the $a_s^{\mathrm{obs}}(n, l)$, and the normalization factor $\nu = M - J$ is the total number of degrees of freedom available to the fit, with M being the total number of data points (here the $a_s^{\mathrm{obs}}(n, l)$), and J the number of fitting parameters ($J = 6$ here). Under this normalization $\chi^2 \lesssim 1$ indicates an adequate fit.

Clearly whatever "best fit" solution one may obtain is, at best, as meaningful as the adopted parameterization for $\Omega(r, \theta)$ can accurately describe the real solar internal rotation profile. Figure X shows a rotation profile constructed using eqs. (12)—(14), with parameter values $\Omega_C/2\pi = 432.8\,\mathrm{nHz}$, $\Omega_{Eq}/2\pi = 460.7\,\mathrm{nHz}$, $c_1 = -62.69\,\mathrm{nHz}$, $c_2 = -67.13\,\mathrm{nHz}$, $r_C = 0.713R_\odot$, and $w = 0.025R_\odot$. Comparing this to Figs. XX and YY, it is clear —and not surprising— that our adopted 6-parameter functional form cannot reproduce all the structures present in the formal 2-D inversions, in particular in the convective envelope. However, it does catch many of its salient large-scale features, such as:

(1) A convective envelope where the differential rotation is primarily in the latitudinal direction, and characterized by equatorial acceleration,
(2) A deep radiative core that rotates very nearly rigidly, at a rate corresponding to the surface mid-latitudes,
(3) A matching of the core and envelope rotation profiles occurring across a thin transition layer located immediately beneath the convective envelope.

Perhaps the most constraining assumption implied by eqs. (12)—(14) is that the transition layer defined by eq. (14) is by construction strictly spherical, with a thickness that is independent of latitude. The inversions of §2 do suggest a slightly prolate form for the shear layer. We will defer consideration of this matter to §4 below, and proceed for now with eq. (14).

It can be expected that rotation profiles described by eqs. (11)—(13) generated using values of w much smaller than the radial width at $r = r_c$ of the integration Kernels in eq. (15) will produce frequency splittings that are effectively identical. We have verified, by direct forward calculation, that with our adopted Kernel set and spatial mesh, solar-like rotation profiles (cf. Fig. 1) yield distinguishable sets of splitting coefficients as long as $w/R_\odot \lesssim 0.005$—0.01. The precise value of the lower limit turns out to depend on whether r_c lies near or far from a spatial mesh point.

3.2 Genetic forward modeling

Having introduced a parameterization for the rotation profile, the modeling task is then treated as a nonlinear least-squares minimization problem. In practice this is a hard minimization problem, chiefly because the quantity to be minimized, χ^2, turns out to be a markedly multimodal functional form in the 6-D search space, so that a *global* (rather than *local*) minimization technique is required.

In a recent paper (Charbonneau *et al.*, 1997) we have described one such technique, based on a genetic algorithm (Holland, 1975; Goldberg, 1989; Charbonneau 1995; and references therein), which we named *genetic forward modeling*. In essence, the method generates a series of *trial solutions* to the minimization problem, and generates sequences of improved trial solutions through operators and selection mechanisms inspired by the biological process of evolution by means of natural selection. An attractive operational feature of the method is that no derivatives of the merit function (here χ^2) with respect to model parameter are needed, so that the linearity —or lack thereof— of the relationship between χ^2 and the defining parameters of the rotation profile does not affect the structure of the algorithm. The interested reader is referred to the above-cited papers for further details.

Genetic algorithm-based methods typically perform minimization in a *bounded* search space; in view of the inversion results of §1, in what follows we restrict the fitting parameters to the ranges:

$$\mathbf{a} \rightarrow \begin{cases} 0 \leq \Omega_C/(2\pi) < 1000 & [\text{nHz}] \text{ Core rotation} \\ 0 \leq \Omega_{Eq}/(2\pi) < 1000 & [\text{nHz}] \text{ Surface equatorial rotation} \\ -200 \leq c_1/(2\pi) < 0 & [\text{nHz}] \text{ Surface differential rotation} \\ -200 \leq c_2/(2\pi) < 0 & [\text{nHz}] \text{ Surface differential rotation} \\ 0.6 \leq r_c < 0.8 & [R_\odot] \text{ Shear layer radial depth} \\ 0.004 \leq w < 0.125 & [R_\odot] \text{ Shear layer thickness} \end{cases} \tag{17}$$

In obtaining the results discussed below we have made one addition to the genetic forward modeling procedure described in Charbonneau *et al.* (1997): the "best fit" solution produced by using the genetic algorithm to evolve a population of 50 trial solutions over 750 generations is used as an input for further minimization using the downhill simplex method, specifically the subroutine `amoeba` described in §XX.YY Press *et al.* (1992). This is straightforward to implement, since in the present context the simplex method also functions as a forward technique, and requires no derivative information. The idea is to run the genetic algorithm until the global minimum in 6-D parameter space has been located, and then switch to the simplex method to rapidly improve the accuracy of the best fit solution. The resulting hybrid technique combines the global exploratory capabilities of genetic algorithms with the faster convergence of the simplex method in the vicinity of the global minimum.

As a further independent safety check on global convergence, we have also computed forward solutions using simulated annealing (Metropolis *et al.*, 196X; Press *et al.*, 1992, §X.Y), rather than genetic algorithms, in tackling the global χ^2 minimization problem. Specifically, we have been using Press *et al.*'s `ametsa` subroutine, itself built around the downhill simplex method mentioned previously. At least for the annealing schedules we have been working with, the simulated annealing-based forward technique fails to converge for a significant ($\sim 33\%$) fraction of trials. However, when it does, convergence is about 50% faster, and the resulting solution very nearly always identical to that obtained by genetic forward modeling.

3.3 Results for Synthetic test cases

Our first task to ascertain whether the "ideal" resolution limit on w ($w \lesssim 0.005$—0.01) mentioned in §X.Y is actually attainable in the presence of noise, and to obtain error estimates for inferred solution parameters. To this end we have constructed a series of rotation profiles for parameter values (Ω_c, Ω_{Eq}, c_1, c_2 and r_c) as for the rotation profile of Fig. 3(A), but with various values of w in the range $0.01 \leq w/R_\odot \leq 0.1$. For each rotation profile we then calculated ten sets of synthetic frequency splitting coefficients (a_1, a_3 and a_5), each for a distinct noise realization added to the splitting coefficients, at a level corresponding to the coefficients determined from the LOWL 2-year dataset. Since the focus of our modeling effort is the solar tachocline, only the modes with inner turning point within $0.5 \leq r/R_\odot \leq 0.8$ were retained. This left 308 (n, l) multiplets with degrees in the range $15 \leq l \leq 65$, $6 \leq n \leq 16$. When then applied our genetic forward modeling procedure to each dataset.

Figure 4 shows the resulting inferred parameter values, as a function of the shear layer thickness parameter w. For a given value of w, each solid dot is the average of the parameter values obtained for each of the 10 different noise realization. The error bar is the one-σ standard deviation of the 10-run set about that mean. The horizontal dotted line indicated the corresponding parameter actually used to construct the synthetic datasets. The surface rotation parameters (Ω_{eq}, c_1 and c_2) are recovered with very high accuracy for all values of w. The core rotation rate Ω_c is also well recovered, even though our mode set excludes the lower ℓ modes having turning points below $r/R_\odot = 0.5$. The location and thickness of the tachocline are recovered with reasonable accuracy down to a thickness $w/R_\odot \simeq 0.04$. Below this thickness the recovered averages for r_c and w deviate significantly from the true values, and the deviation about the mean increases sharply. This indicates that data noise is affecting significantly the determination of r_c and w.

[**In what follows if Mike and Jorgen have not discussed the meaning of the** a **coefficents, I'll elaborate a bit more**] For most of the modes retained in our dataset, the a_1 coefficients —effectively a latitudinally- averaged measured of the rotation rate— are determined with much greater relative accuracy ($\lesssim 0.5\,\%$) than either the a_3 (accurate to $\lesssim 10\,\%$) or a_5 coefficients. This implies that the χ^2 minimization is largely driven by the need to accurately reproduced the a_1 coefficients. This is why the parameters Ω_{eq} and Ω_c are so well recovered on Figure 4. In order to increase the accuracy of our determinations of r_c and w, we now consider inversions making use of the a_3 coefficients only. These effectively correspond to the first θ-dependent term in a latitudinal expansion of the differential rotation profile; the a_3 coefficients can then be expected to be sensitive to the change from approximately constant latitudinal differential rotation in the convective envelope to vanishing differential rotation in the underlying radiative core. However, the fit is now no longer as sentitive to the zero point of the rotation profile as when the a_1's are included in the χ^2 calculation.

Figure 5 shows the values of r_c and w recovered by this reduced fitting procedure, again for various values of the shear layer thickness w. Comparing this to parts (E) and (F) of Fig. 4, one notes that the central estimates for those two parameters lie now closer to the true values, and that the error bars are generally smaller than on Fig. 4(E) and (F). Furthermore, in terms of tachocline structure, the solutions now retain useful accuracy down to $w/R_\odot \simeq 0.03$, which is a small but significant improvement over the solutions shown on Fig. 4.

It may argue that the results discuss above give an overly optimistic evaluation of the spatial resolution capabilities of the forward modeling scheme. Such a claim can legitimately be made on the grounds that the above parameter recovery exercise made use of the same parameterization for $\Omega(r, \theta)$ than was used to generate the synthetic datasets in the first place. Of course we should not count on being that lucky in applying the technique to real data, so one should not assume *a priori* that the resolution capabilities of the method estimated from Figs. 4 and 5, carries over to real data. To test this possibility we have computed a second series of forward modeling solutions, using the same synthetic splitting dataset as before, but this time assuming 2-parameter functional forms for the radial dependency of the shear layer, i.e., the function $f(r)$, different from eq. (13). Specifically, we used the sigmoid and cosine bell functions:

$$g(r;r_c,w) = 1 - \left[1 + \exp\left(\frac{r - r_C}{0.1875\,w}\right)\right]^{-1} \tag{18a}$$

$$h(r;r_c,w) = \begin{cases} 0 & r < r_c - w/2, \\ \frac{1}{2}\left[1 - \sin\left(\frac{\pi}{2}\frac{r-r_C}{0.925\,w}\right)\right] & r_c - w/2 \leq r \leq r_c + w/2, \\ 1 & r > r_c + w/2, \end{cases} \tag{18b}$$

The numerical factors multiplying w in eqs. (18) are chosen so that, in the range $0.01 \leq w/R_\odot \leq 0.1$, the corresponding radial shear profiles have very nearly the same full widths at half maximum as given by eq. (13) for the same value of w. Repeating the parameter recovery exercises produces solutions with accuracy comparable to those obtained previously when eq. (18a) is used, and slightly less accurate if eq. (18b) is used instead. Nevertheless, all solutions retain useful accuracy down to $w/R_\odot \simeq 0.03$—0.04. For reference, note that the sigmoid function is the parameterization used by Basu (1997).

3.4 Results for LOWL data

We now turn to the application of genetic forward modeling to real data, namely the LOWL 2-year frequency splitting dataset (Schou & Tomczyk, 1997). As with the synthetic data, we only retain the 308 (n,l) multiplets with inner turning points in the range $0.5 \leq r/R_\odot \leq 0.8$.

Consider first the use of the 6-parameters angular velocity profile defined by eqs. (11)—(13). If the full set of coefficients is used (a_1, a_3 and a_5), the best-fit solution has

$$[r_c, w]/R_\odot = [0.703 \pm 0.002, 0.072 \pm 0.017], \qquad \chi^2 = 1.456, \qquad a_1 + a_3 + a_5. \tag{19a}$$

If one uses only the a_3 coefficient, the best-fit is now characterized by

$$[r_c, w]/R_\odot = [0.704 \pm 0.002, 0.050 \pm 0.016], \qquad \chi^2 = 1.482, \qquad a_3 \text{ only}. \tag{19b}$$

The two solutions agree on r_c, in the sense that each solution is well within the other's one σ range. This is not the case with the thickness parameter w, however, indicating that the two determinations of w are mutually incompatible. A further indication that something might be astray come from the fact that the χ^2 for both best fits is significantly larger than one. The bottom line is that we have here a significant discrepancy, which needs to be resolved if we are to assign any confidence to our determination of the tachocline thickness.

3.5 Additional results for LOWL data

The rotation profile in the convective envelope, as defined by our adopted parameterization, is characterized by a radial gradient that strictly vanishes outside of the tachocline. Formal inversions, such as the ones discussed in §2 above, indicate that a weak radial gradient does exist in the envelope, in particular near the surface, and at all depths in the equatorial regions. An improper representation of the rotation profile in the equatorial regions of the envelope can be expected to introduce a significant bias in solutions making use of the a_1 coefficients, since those are particularly sensitive to the equatorial rotation rate. One may envision a situation where, in attempting to fit an outwardly increasing rotation profile in the equatorial part of the envelope, a solution having $\partial\Omega/\partial r \equiv 0$ by construction may attempt to fit the radial gradient by broadening the shear layer. This one possible explanation for the discrepancy noted in the preceding section. In order to explore this possibility we now consider a series of solutions for LOWL data, where the rotation profile in the convective envelope now includes a cylindrical component. Specifically, we replace eq. (12) by

$$\Omega_S(\theta;\Omega_{\rm eq},c_1,c_2) = \Omega_{\rm eq} + c_1\cos^2(\theta) + c_2\cos^4(\theta) + c_3 r\sin(\theta) \qquad (20)$$

which involves the addition of one additional parameter (c_3), setting the amplitude of the cylindrical component. The genetic forward modeling proceeds exactly as before, with the exception that the fit now involves seven, rather than six, fitting parameters. As in §3.4 we perform two fits, the first for all three sets of a coefficients, the second using only the a_3 coefficients. The resulting tachocline best-fit parameters are:

$$[r_c, w]/R_\odot = [0.702\pm0.002, 0.057\pm0.016], \qquad \chi^2 = 1.452, \qquad a_1+a_3+a_5. \quad (21a)$$

and

$$[r_c, w]/R_\odot = [0.705\pm0.002, 0.051\pm0.016], \qquad \chi^2 = 1.482, \qquad a_3 \text{ only}. \quad (21b)$$

The tachocline for the a_3-only best-fit solution is very slightly higher and thicker than its original counterpart (eq. [19b]), although their χ^2's are identical to 4 digits. The solution for the full set of coefficents, however, shows a significant decrease in the inferred value for the tachocline thickness w, which moreover brings it in line with the solution obtained using only the a_3 coefficients. Going from a 6-parameter to a 7-parameter fit has led to a small but significant decrease in the best-fit χ^2's. The differences in the corresponding rotation profiles is subtle, and illustrate how relatively small changes in envelope rotation can have significant effects on the inferred rotation deeper down. The full solution parameter vectors for these two solutions are:

$$[\Omega_c, \Omega_{\rm eq}, c_1, c_2, r_c, w] = [432.7, 460.8, -62.94, -66.97, 0.703, 0.072] \qquad (22a)$$

$$[\Omega_c, \Omega_{\rm eq}, c_1, c_2, c_3, r_c, w] = [432.7, 452.6, -59, 40, -64.07, 8.936, 0.702, 0.057] \qquad (22b)$$

(units as in eq. [17]), and the corresponding rotation profiles are plotted on Figure 6. Note how the profiles differ only slightly in the equatorial regions of the envelope.

Clearly one could further refine the parameterization, to properly reproduce more and more of the smaller spatial scales of the rotation profile in the envelope, gradually reducing the χ^2 to ~ 1 in the process. In the present context this would not be a particularly meaningful exercise. The limited attempt at doing so presented in this section should nonetheless serve as a sobering reminder that we are at the mercy of our parameterization, in much the same was as regularized least-squares inversions are at the mercy of their adopted regularization functional and parameters.

4. Results for models with latitude-dependent shear layers

$$w \to w(\theta) = w_0 + w_1 \cos^2(\theta)$$

$$r_c \to r_c(\theta) = r_{c0} + r_{c1} \cos^2(\theta)$$

5. Conclusion

Solar cycle variations in tachocline structure ?

References

Basu, S. 1997, preprint

Brown, T.M. 1985, Nature, 317, 591

Brown, T.M., & Morrow, C.A. 1987, ApJL, 214, L21

Brown, T.M., Christensen-Dalsgaard, J., Dziembowski, W.A., Goode, P., Gough, D.O., & Morrow, C.A. 1989, ApJ, 343, 526

Charbonneau, P. 1995, ApJS, 101, 309

Charbonneau, P., & MacGregor, K.B. 1996, ApJL, 473, L59

Charbonneau, P., & MacGregor, K.B. 1997, ApJ, XX, in press

Charbonneau, P., Christensen-Dalsgaard, J., Henning, R., Schou, J., Thompson, M.J., & Tomczyk, S. 1997, in IAU Symp. 181: Sounding Solar and Stellar Interiors, eds. J. Provost & F.X. Schmider, in press

Charbonneau, P., & Knapp, B. 1995, A User's Guide to PIKAIA 1.0, NCAR Technical Note 418+IA

Charbonneau, P., Tomczyk, S., Schou, J., & Thompson, M.J. 1997, submitted to ApJ

Christensen-Dalsgaard, J., 1991, in *Challenges to theories of the structure of moderate-mass stars*, *Lecture Notes in Physics*, vol. **388**, eds. Gough, D.O., & Toomre, J., (Heidelberg: Springer), p. 11

Gilman, P.A., & Miller, J. 1986, ApJS, 61, 585

Gilman, P.A., & Fox, P. 1997, ApJ, XX, in press

Glatzmaier, G. 1985, ApJ, 291, 300

Goode, P.R., Dziembowski, W.A., Korzennik, S.G., & Rhodes, E.J. 1991, ApJ, 367, 649

Kitchatinov, L.L., & Rüdiger, G. 1993, Å27696

Kitchatinov, L.L., & Rüdiger, G. 1995, Å299446

Kosovichev, A.G. 1996, ApJL, 469, L61

Parker, E.E. 1993, ApJ, 417?, YY

Press, W.H., Teukolsky, S.A., Vetterling, W.T., & Flannery, B.P. 1992, *Numerical Recipes* (2nd ed.), Cambridge University Press.

Ritzwoller & Lavely, ApJ, 369, 557

Rüdiger, G., & Brandenburg, A. 1995, ApJ, 296, 557

Rüdiger, G., & Kitchatinov, L.L. 1997, Astr. Nach., XXX, YYY

Schou, J., Christensen-Dalsgaard, J., & Thompson, M.J. 1992, ApJL, 385, L59

Schou, J., Christensen-Dalsgaard, J., & Thompson, M.J. 1994, ApJL, 433, 389

Schou, J., & Tomczyk, S. 1997, ApJS, in preparation

Schüssler, M. 1996, in *Solar and Astrophysical MHD Flows*, NATO ASI, vol. C481, ed. K.C. Tsinganos, 17.
Spiegel, E.A., & Zahn, J.-P. 1992, Å265106
Tobias, S. 1996, ApJ, XX, YY
Tomczyk, S., Schou, J., and Thompson, M.J. 1995b, ApJL, 448, L57

Figure captions

Figure 3: Panels (A) and (C): Regularized least-square inversion of the LOWL dataset, shown as radial cut at three latitudes (part (A)) and as isocontours of angular frequency (part (C);

Figure 4: Results for synthetic test cases. Each panel shows the recovered value for one of the six parameters defining the rotation profile given by eqs. (11)—(13), as a function of the w-value used to contruct the synthetic datasets. Each solid dot is a average of 10 runs, each carried out with a different noise realization added to the synthetic splitting coefficients. The error bars are estimated *a posteriori* by computing the standard deviation about the mean parameter value for each set of 10 runs, and so give a Monte Carlo-like measure of the influence of noise on the accuracy of recovered parameter values.

Figure 5: Recovery of r_c and w for the synthetic test cases, when only the a_3 coefficients are used to constrain the fit. This Figure should be compared to parts (E) and (F) of Figure 4.

Figure 6: Two "Best fit" rotation profiles obtained from (A) the 6-parameter fit defined by eqs. (12)—(14), amd (B) the 7-parameter fit defined by replacing eq. (XX) by eq. (YY). Both solutions were obtained using the a_1, a_3 and a_5 splitting coefficients. The inclusion of a low amplitude cylindrical component to the rotation profile in the envelope leads to a tachocline having thickness $w \simeq 0.05$, in agreement with the thickness inferred from either 6- or 7-parameter fits using onlt the a_3 splitting coefficients (see text).

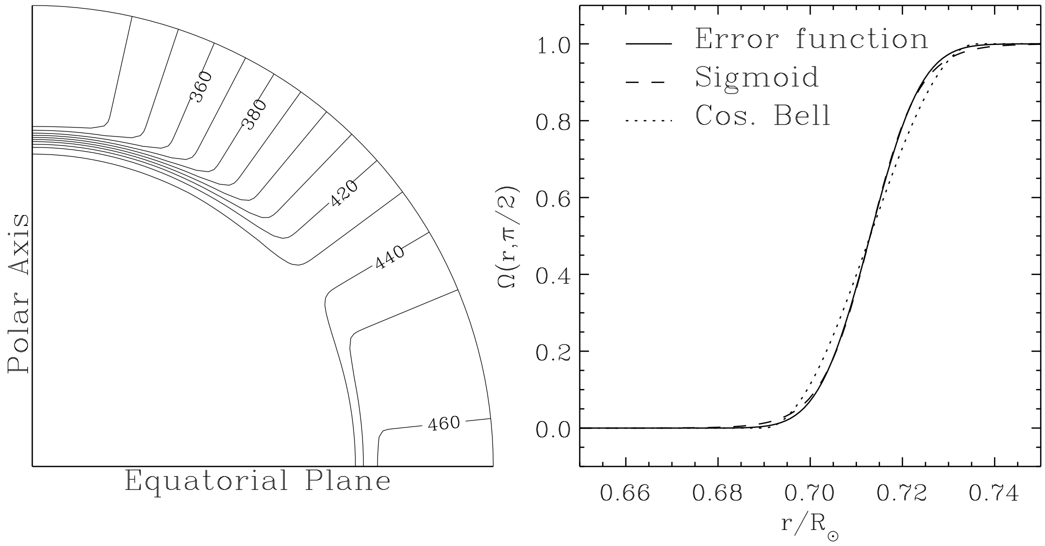

360
380
420
440
460
Polar Axis
Equatorial Plane
Error function
Sigmoid
Cos. Bell
1.0
0.8
0.6
0.4
0.2
0.0
$\Omega(r,\pi/2)$
0.66
0.68
0.70
0.72
0.74
$r/R_\odot$

Figure 3

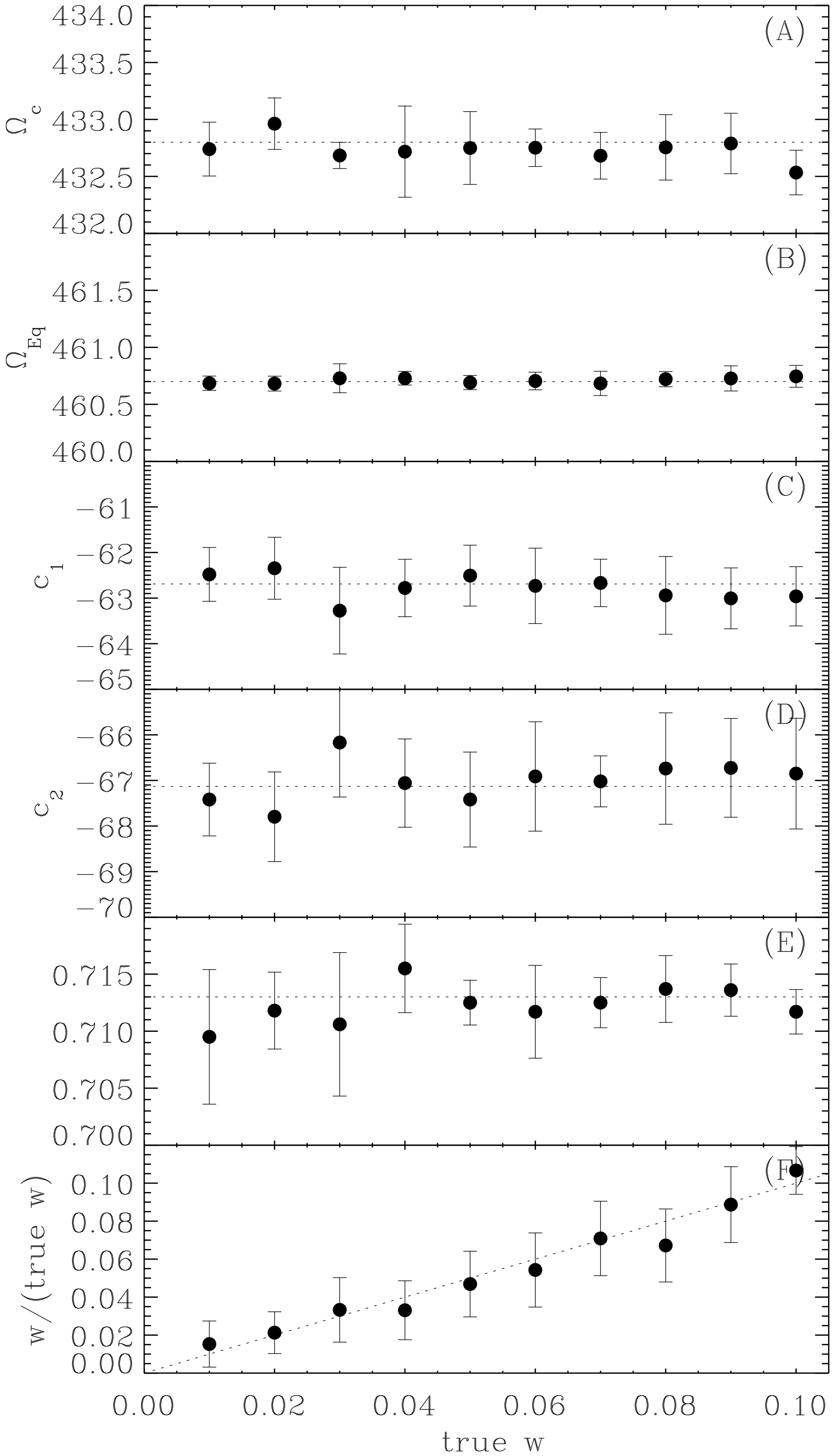

(A)
(B)
(C)
(D)
(E)
(F)
Ω_c
Ω_{Eq}
c_1
c_2
w/(true w)
true w
434.0
433.5
433.0
432.5
432.0
461.5
461.0
460.5
460.0
−61
−62
−63
−64
−65
−66
−67
−68
−69
−70
0.715
0.710
0.705
0.700
0.10
0.08
0.06
0.04
0.02
0.00
0.00
0.02
0.04
0.06
0.08
0.10

Figure 4

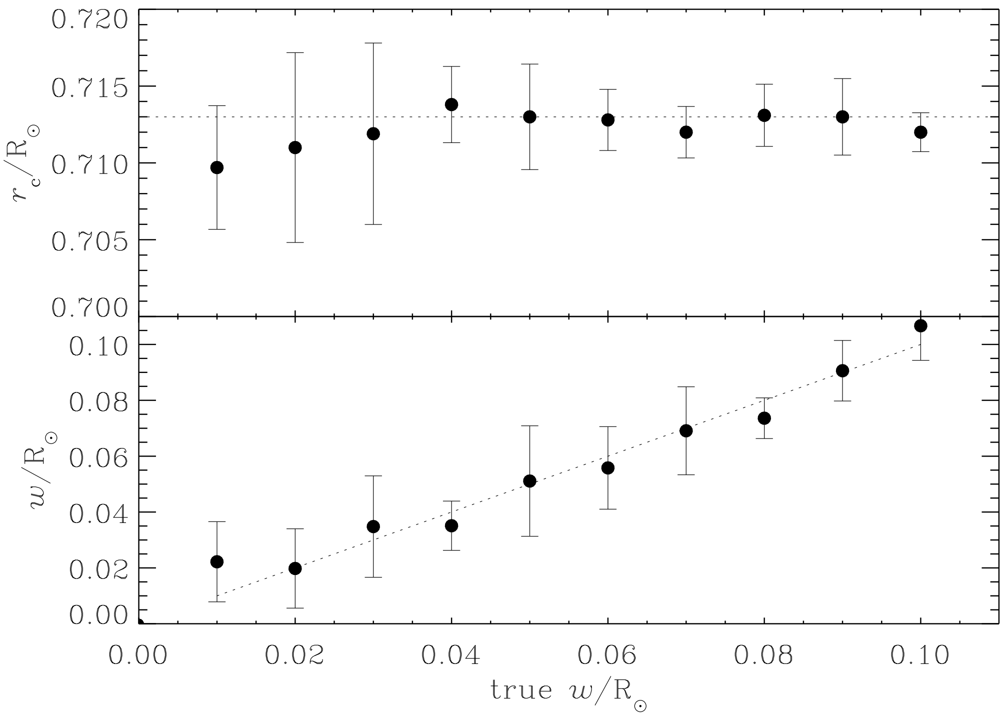
0.720
0.715
0.710
0.705
0.700
$r_c/R_\odot$
0.10
0.08
0.06
0.04
0.02
0.00
$w/R_\odot$
0.00
0.02
0.04
0.06
0.08
0.10
true $w/R_\odot$

Figure 5

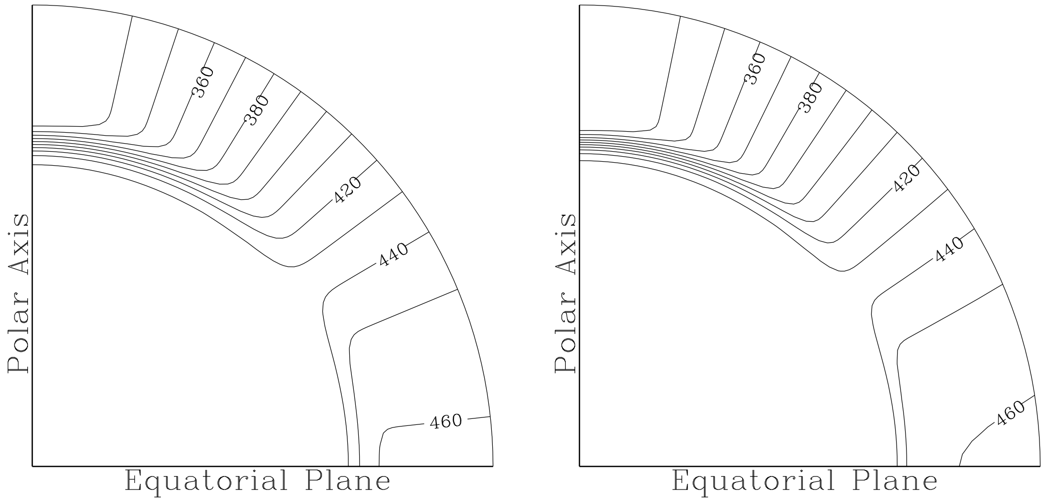
360
380
420
440
460
Polar Axis
Equatorial Plane
360
380
420
440
460
Polar Axis
Equatorial Plane

Figure 6